Biomaterials Science

ROYAL SOCIETY OF CHEMISTRY

PAPER

View Article Online
View Journal | View Issue

Cite this: *Biomater. Sci.*, 2025, **13**, 4803

Biomimetic vascular scaffolds *via* hybrid 3D printing-phase separation for vascularized cardiac tissue with enhanced perfusion and maturation†

Xinyao Pan,‡[a] Sitian Liu,‡[a] Meng Long,‡[a] Ruijun Peng,[b] Lanlan Hu,[c] Liu Yu[a] and Wenhua Huang*[a]

Received 14th May 2025,
Accepted 27th June 2025

DOI: 10.1039/d5bm00734h

rsc.li/biomaterials-science

Cardiac tissue engineering (CTE) shows great potential for repairing chronic myocardial damage. However, inadequate vascularization in engineered myocardial constructs thicker than 200 μm limits nutrient perfusion and leads to core necrosis, restricting its clinical application. Here, we combine 3D printing with phase separation to fabricate biomimetic vascular scaffolds, polycaprolactone (PCL) tubes, exhibiting enhanced mechanical resilience and biocompatibility. The PCL-tube facilitates the self-assembly of human umbilical vein endothelial cells (HUVECs) into microvascular networks that recapitulate the barrier functions of native vasculature, enabling selective molecular transport while preserving structural integrity. The endothelialized PCL-tube (ECs-PCL-tube) is integrated with cardiomyocyte (CM)-loaded fibrinogen-GelMA (FG) hydrogel through modular assembly to form a multi-scale, vascularized engineered cardiac tissue. The results show that the ECs-PCL-tubes significantly improve cell viability and enhance nutrient perfusion efficiency. Furthermore, the vascularized engineered cardiac tissue exhibited superior CM sarcomere formation, gap junction expression, and contractility, promoting enhanced cell–cell communication. In summary, our study addresses the limitations of lumen collapse and nutrient diffusion in conventional hydrogel systems, offering a scalable and cost-effective solution for constructing functional, vascularized cardiac tissues. This approach holds significant potential for applications in regenerative medicine and drug screening.

1 Introduction

Cardiovascular diseases (CVDs) remain the leading cause of global mortality, with myocardial infarction (MI) alone leading to irreversible cardiomyocyte loss and fibrotic scarring, ultimately progressing to heart failure.[1,2] Although current treatments including myocardial repair and heart transplantation have shown potential applications, they still face significant limitations. The effectiveness of these treatments is hindered by a shortage of donor organs and tissues. Cardiac tissue engineering (CTE) offers promise for repairing the damaged myocardium.[3–6] For instance, *in vitro* engineered cardiac tissues were developed and subsequently implanted into cardiac tissue defects for treatment.[7,8] However, tissues thicker than 200 μm require an efficient vascular network to maintain survival, as nutrient and oxygen diffusion become inadequate at greater depths.[9,10] Without a sufficient vascular network, the large-scale engineered myocardium struggles to maintain a nutrient and oxygen supply, leading to cell death and tissue necrosis.

To fulfill this essential requirement, researchers have developed several types of vascular scaffolds *in vitro*.[11–14] Despite these advances, most models fail to replicate the hierarchical complexity of natural vasculature, which is crucial for ensuring proper perfusion in thicker tissues.[15–18] This limitation underscores the necessity of vascularization for sustaining cell viability in clinically relevant tissue volumes.[3,19,20] Several advanced techniques such as embedded bioprinting[21,22] and Digital Light Processing (DLP) printing[23] have been used to prepare bionic vascular networks. For instance, bionic vascular networks have been embedded into functional cardiac tissue *via* coaxial sacrificial printing.[24] Although advanced techniques such as embedded bioprinting and DLP printing enable

[a]*Guangdong Engineering Research Center for Translation of Medical 3D Printing Application, Guangdong Provincial Key Laboratory of Medical Biomechanics, Department of Human Anatomy, School of Basic Medical Sciences, Southern Medical University, Guangzhou, 510515, China. E-mail: hwh@smu.edu.cn*
[b]*Biomaterials Research Center, School of Biomedical Engineering, Southern Medical University, Guangzhou, 510515, P.R. China*
[c]*State Key Laboratory of Organ Failure Research, Department of Cardiology, Nanfang Hospital, Southern Medical University, Guangzhou, 510515, China*
†Electronic supplementary information (ESI) available. See DOI: https://doi.org/10.1039/d5bm00734h
‡These authors contributed equally to this work.

precise vascular patterning, their reliance on costly equipment and lack of scalability hinder their potential for widespread clinical applications.[25–28] Additionally, hydrogel-based channels, despite their inherent biocompatibility, limit their long-term applications due to their low mechanical strength and swelling properties.[29] This limitation leads to lumen collapse and deformation, which severely hampers their ability to maintain stable vascular network perfusion.[30,31] Thus, there is an urgent need to develop stable, biomimetic vascular scaffolds that synergize engineering precision with biological self-organization to sustain the thick engineered myocardium.

To address these challenges, researchers have employed sacrificial materials in combination with 3D printing technologies, enabling the fabrication of vascular scaffolds with complex geometries and precise structural control.[32] While this method allows for precise control over scaffold structures and enables the creation of intricate vascular networks, significant limitations persist. Existing approaches struggle to establish hierarchical vascular networks that simultaneously support macroscale perfusion and microscale nutrient exchange—a critical requirement for engineering functional cardiac tissues. Several advanced methods have been developed for constructing multiscale vascular networks *in vitro*.[33–35] However, these approaches often depend on complex fabrication workflows and specialized instrumentation, hindering the scalability and reproducibility of biomimetic vasculature. Phase separation is an efficient and rapid method for fabricating porous structures.[36,37] Previous studies have used this technique combined with sacrificial materials to fabricate vascular networks *in vitro*.[32] Therefore, we hypoth-

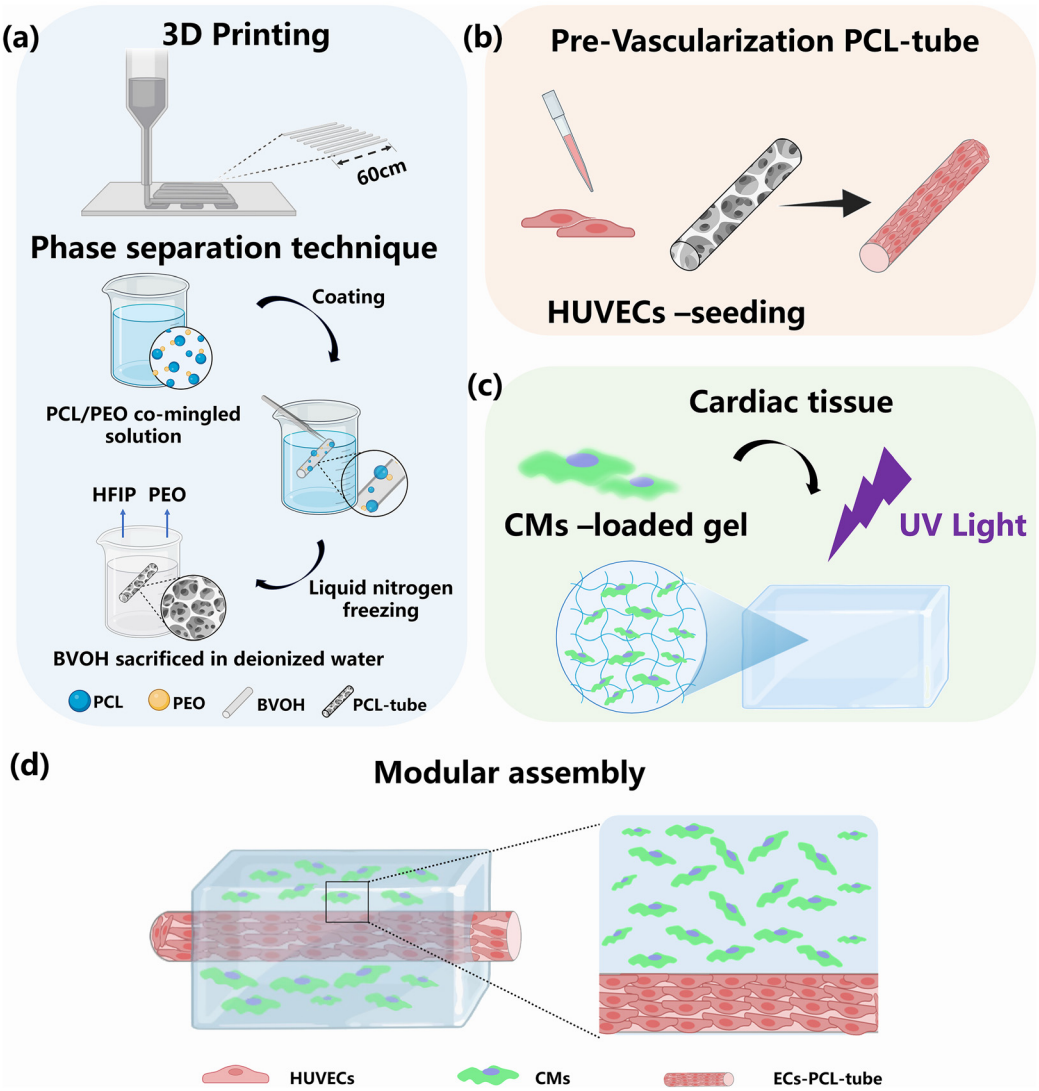

Fig. 1 Schematic of the design and fabrication of the biomimetic vascularized cardiac tissue structure. (a) Fabrication of the PCL-tube integrated with 3D printing and the phase separation technique; (b) combination with HUVECs to form multi-scale pre-vascularized scaffolds. (c) Scheme showing the use of FG hydrogels for the preparation of engineered cardiac tissue scaffolds for inducing engineered cardiac tissue growth *in vitro*. (d) Modular assembly strategy for fabricating multiscale vascularized functional engineered cardiac tissue.

esized that combining 3D printing and phase separation technology could provide a promising approach for fabricating hierarchical vascular networks, which would enable the creation of a microenvironment to support the self-assembly of HUVECs and maintain stable lumens.

Herein, we employed a combined 3D printing-phase separation process to fabricate large vascular scaffolds using polycaprolactone (PCL) tubes (Fig. 1a). We further developed a multi-scale vascular scaffold (named ECs-PCL-tube) by leveraging the self-assembling properties of human umbilical vein endothelial cells (HUVECs) (Fig. 1b). PCL-tubes with excellent mechanical properties, biocompatibility, and porous surfaces overcame the issue of hollow tubes within hydrogels, which were prone to collapse and clogging due to insufficient mechanical strength. Cardiomyocyte (CM)-laden fibrinogen-GelMA (FG) hydrogels served as the engineered cardiac tissue core (Fig. 1c). More importantly, these PCL-tubes were modularly assembled with engineered cardiac tissue to construct multi-scale vascularized engineered cardiac tissue to address the necrosis of engineered cardiac tissue from inadequate central nutrient perfusion in 3D cultures, confirming that ECs-PCL-tubes promoted the development of CMs and facilitated intercellular communication (Fig. 1d). Furthermore, the modular assembly approach shows great promise for constructing vascularized networks within engineered cardiac tissues and for preparing *in vitro* models of vascularized cardiac tissue.

2 Materials and methods

2.1 Preparation and characterization of PCL-tubes

Phase separation strategies have been developed based on previous studies.[38] The raw materials for phase separation consisted of a mixture of PCL (M_n = 80 kDa, Sigma-Aldrich) and polyethylene oxide (PEO), with hexafluoroisopropanol (HFIP) serving as the solvent. The mixture was magnetically stirred at 50 °C for 12 h to obtain the PCL/PEO co-mingled working solution. Four distinct PCL concentrations (60, 70, 80, and 90 mg mL^{-1}, designated as 6%, 7%, 8%, and 9% PCL-tube systems) were blended with a fixed PEO concentration of 50 mg mL^{-1} in the co-mingled solutions. Shapr3D design software was used to create a model of a 1.5 mm diameter tube made from the water-soluble sacrificial material butylene glycol vinyl alcohol copolymer (BVOH). Then, the BVOH sacrificial scaffolds were printed with a fused deposition 3D printer (Guangzhou Jiazhi Joint Technology Co., Ltd). The PCL/PEO working solution was coated onto the BVOH sacrificial scaffolds in a fume hood and then transferred immediately to a −80 °C freezer for freezing. After 1 h, the samples were removed and immersed in liquid nitrogen for 5 min to induce the reactions. Subsequently, the samples were placed in deionized water to dissolve the BVOH, a process that typically required 1–2 days. Optimal cutting temperature compound (OCT) embedding agent was applied to the PCL-tubes, followed by freezing and sectioning both cross-sectionally and longitudinally using a freezing microtome (Leica). Scanning electron microscopy (SEM) was used to capture images of the micro-morphology and cross-section of the PCL-tubes at different concentrations. Porosity was analyzed using ImageJ software.

2.2 *In vitro* cytocompatibility of PCL-tubes

The cytocompatibility of the PCL-tube was assessed using live/dead immunofluorescence staining. Before cell seeding, 6% PCL-tubes were soaked in 75% ethanol for 12 h. The tubes were then rinsed thoroughly with Dulbecco's phosphate-buffered saline (DPBS). HUVECs were encapsulated on scaffolds with a cell density of 3×10^5 mL^{-1} in 0.1 mL and cultured for 24 h in a high-glucose medium (Gibco) supplemented with 10% (v/v) fetal bovine serum (FBS, Gibco) and 1% (v/v) penicillin–streptomycin (P/S, Gibco) at 37 °C and 5% CO_2. Cell viability was assessed using a Live/Dead Viability Assay Kit. After staining with calcein-AM/propidium iodide for 30 min, cells were observed under a confocal laser scanning microscope (Nikon Co., Ltd, Japan) to visualize green (live cells) and red fluorescence (dead cells).

2.3 Immunostaining of endothelial monolayers

HUVECs were seeded into the PCL-tubes at a low cell density (0.1 mL, 1×10^6 cells per mL) and cultured for 72 h in Dulbecco's modified Eagle's medium (DMEM high glucose, L-glutamine, Gibco) containing 10% (v/v) FBS (Gibco) and 1% (v/v) P/S (Gibco) at 37 °C and 5% CO_2. After 72 h of culture, immunostaining with Platelet Endothelial Cell Adhesion Molecule-1 (CD31) and vascular endothelial cadherin (VE-cadherin) antibodies was performed on the PCL-tube to examine intercellular connections and the endothelialization function of the endothelial monolayer within the microchannels. The ECs-PCL-tubes were fixed in 4% paraformaldehyde for 30 min and soaked in 0.1% Triton X-100 for 40 min to permeabilize the cell membrane. After permeabilization, these tubes were blocked with 1% bovine serum albumin (BSA, Sigma-Aldrich) in PBS for 2 hours at room temperature. They were then incubated overnight with CD31 (1 : 500 dilution) and VE-cadherin (1 : 500 dilution) primary antibodies at 4 °C. Then, the tubes were incubated with Alexa Fluor 488-conjugated donkey anti-rabbit secondary antibody (1 : 1000 dilution) for 3 h at room temperature (25 °C). These tubes were then stained with DAPI (1 : 1000 dilution) for 30 min. All reagents were injected into the lumen to ensure optimal contact and reactions. Additionally, the images were captured using confocal laser scanning microscopy (ZEISS Axio Observer A1). HUVECs were routinely passaged in tissue culture flasks and used before the eighth passage to preserve key endothelial characteristics.

2.4 Barrier function of ECs-PCL-tubes

The validation of the barrier function of ECs-PCL-tubes was referenced from previous studies.[29,39] To assess the barrier function of the endothelialized micro-vascular network, ECs-PCL-tubes were embedded within methacrylate gelatin (GelMA) and permeability assays were performed using 70 kDa FITC-dextran. GelMA was synthesized following our previous study.[40] PCL-tubes were embedded within GelMA as a control

group and positioned on a fluorescence microscope (WMF-3690, Shanghai Wumo Optical Instruments Co., Ltd). Fluorescein isothiocyanate–dextran (FITC-dextran, Sigma-Aldrich) with a molecular weight of 70 kDa was injected into the PCL-tube at a concentration of 500 μg mL^{-1}. The movement of FITC-dextran within two sets of channels was captured in diffusion images by fluorescence microscopy. Time-lapse imaging acquired fluorescence data at 15 min intervals from 5 to 50 min post-perfusion. Permeability differences were clearly observed at the end of the assay (t = 50 min) by the amount of dextran diffused into GelMA. The diffusion of FITC-dextran was observed and recorded. The images were converted to grayscale and quantitatively analyzed using ImageJ software.

2.5 CM culture within FG hydrogels

CMs were isolated following the previous method.[41] The CMs were cultured in accordance with the Institutional Animal Ethics Committee guidelines of Southern Medical University. Engineered myocardial tissue was prepared by inoculating cardiomyocytes in FG hydrogels for 5 days in culture. The FG hydrogel solution was prepared by dissolving GelMA, the photoinitiator lithium phenyl (2,4,6-trimethylbenzoyl) phosphinate (LAP) (StemEasy, China), fibrinogen (Sigma-Aldrich, USA), and thrombin (Sigma-Aldrich, USA) at room temperature. The final concentrations of GelMA, LAP, fibrinogen, and thrombin were 5%, 0.2%, 1% (w/w), and 5 U mL^{-1}, respectively. After trypsin digestion of the primary CMs, they were resuspended in the FG hydrogel solution (2×10^5 cells per mL). LAP (0.2% weight percent) was combined with FG hydrogel containing CMs. The slides were then quickly exposed to 405 nm UV light, and the FG hydrogel solution was photopolymerized for 5 seconds. The UV-crosslinked FG hydrogels were then incubated for 3 min at 37 °C to crosslink fibrinogen and create a crosslinked fibrin network.

2.6 Immunostaining

PCL-tubes and ECs-PCL-tubes were assembled with CM-laden FG hydrogels, named Tube-Gel and ECs-Tube-Gel. CM-laden FG hydrogels served as the control group (named Gel). Cellular viability was investigated using a live/dead viability kit to assess the cell viability of all groups. After being cultured for 5 days, the CM-laden FG hydrogels were washed with DPBS 3 times and treated with ethidium homodimer-1 (0.5 μM) and Calcein AM (0.25 μM) for 45 min. After staining, the samples were observed under a confocal laser scanning microscope. ImageJ was utilized to analyze the number of live cells from 3 randomly selected areas of 3 samples for each group. Furthermore, phalloidin staining (Invitrogen, USA) was used to visualize F-actin and evaluate cellular spreading after 5 days of culture. These samples were fixed for 30 min in 4% paraformaldehyde solution and then permeabilized with 0.2% Triton X-100 solution for 40 min. After being blocked in 1% BSA in DPBS for 2 h, the cell constructs were incubated with F-actin (1 : 500 dilution) at room temperature for 2 h. Subsequently, the nuclei were counterstained with DAPI. Fluorescence images of these stained samples were obtained using a confocal laser scanning microscope. The myocardial maturation was evaluated using alpha-actinin (α-actinin), Connexin 43 (CX43), and cardiac troponin (cTnT) staining after 5 days of culture. Briefly, samples were stained with two primary antibodies, including α-actinin and CX43, at a 1 : 500 dilution in 1% BSA in DPBS overnight at 4 °C. Alexa Fluor-488 conjugated secondary antibody for α-actinin and Alexa Fluor-555 conjugated secondary antibody for CX43 were then added and incubated for 2 h at room temperature (25 °C). Finally, all samples were counterstained with DAPI to detect the nuclei. Cell attachment, morphology, and distribution were observed using a confocal laser scanning microscope. Fluorescence images of these stained samples were captured using confocal laser scanning microscopy. The characterization of cTnT was then performed using the same experimental steps described above, and the presence of CD31 in the ECs-Tube-Gel group was localized.

2.7 Statistical analysis

The experiment was performed at least three times for each sample (per sample, $N \geq 3$), and the results were expressed as mean ± standard deviation. An independent sample t-test was used for statistical analysis of all experimental data, and differences were considered statistically significant as $P < 0.05$. Data were analyzed using ImageJ and Origin software.

3 Results and discussion

3.1 PCL-tube preparation using 3D printing–phase separation hybrid fabrication

We fabricated a bionic vascular scaffold PCL-tube using a hybrid fabrication approach based on 3D printing and phase separation. The fabrication scheme is shown in Fig. 1a. Briefly, the PCL-tube was fabricated by coating the PCL/PEO co-hybrid solution onto BVOH sacrificial scaffolds. After freezing, PCL-tubes with pores were created by dissolving the BVOH sacrificial scaffolds in water. PCL has been widely recognized for its excellent biocompatibility and mechanical properties, making it ideal for scaffold fabrication, especially in supporting hollow tubes and preventing collapse.[42–44] As a hydrophobic polymer, the phase continuity of PCL during phase separation resulted in slower solvent exchange rates.[45] To overcome this drawback, PEO was incorporated to accelerate the solvent exchange rate and enhance the hydrophilicity of the resulting composite, thereby improving the overall material properties.[45–47] As shown in Fig. 2a, we selected a 1.5 mm diameter for printing the BVOH sacrificial scaffolds, as it matched the typical size of small arteries in the human cardiovascular system, ensuring proper blood perfusion and mimicking natural vasculature.[48] The printed BVOH sacrificial scaffolds shown in Fig. 2b illustrate the high precision and fidelity of the printing process. To enhance the structural integrity and mechanical properties of the vascular scaffolds, we tested PCL concentrations ranging from 60 mg mL^{-1} to 90 mg mL^{-1} and named them 6% PCL, 7% PCL, 8% PCL and 9% PCL, respectively. These concen-

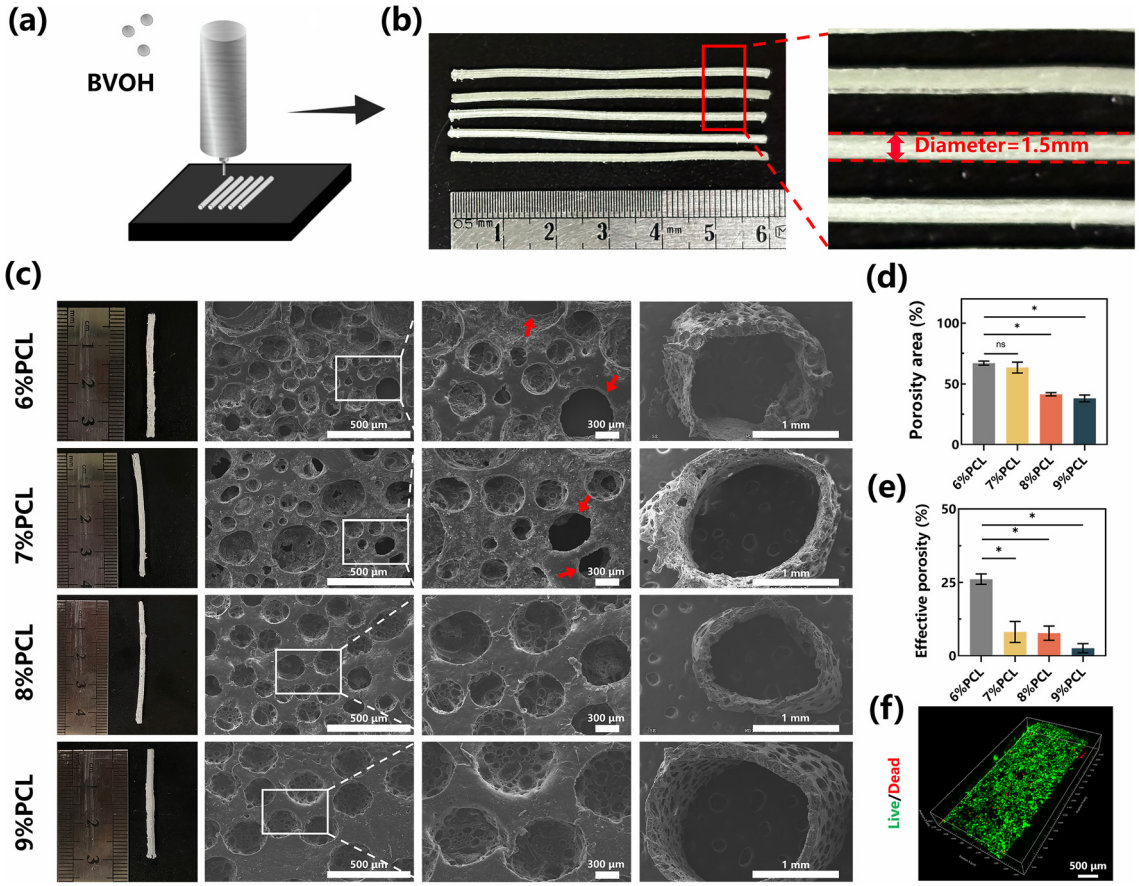

Fig. 2 Fabrication and characterization of the PCL-tube integrated with 3D printing and the phase separation technique. (a) Schematic of a BVOH sacrificial scaffold prepared by fused deposition printing. (b) Optical photograph of the BVOH sacrificial vascular scaffold. (c) Physical representations and SEM images of the PCL-tube at different concentrations, including the tube wall and cross-section. Red arrows indicate the effective pores. (d) Statistical analysis of the porosity of the PCL-tube at different concentrations (n = 3). (e) Statistical analysis of the effective porosity of the PCL-tube at different concentrations (n = 3). (f) Live/Dead images showing that HUVECs grew normally on the PCL-tube scaffolds (*p < 0.05).

trations were chosen to balance sufficient tube wall thickness with the formation of penetrating pores, essential for preventing collapse while maintaining structural stability. After the BVOH sacrificial scaffold was removed, the SEM images showed that all four concentrations formed PCL-tubes with a hollow cavity with a circular or elliptical shape and the presence of pores in the wall of the PCL-tubes (Fig. 2c). Despite localized deformation of the luminal structure induced by cryo-sectioning-induced mechanical stress, the 6% PCL scaffold retained a circular cavity morphology and dimensional integrity (1.5 mm). Porosity of the PCL-tube was further analyzed, revealing higher porosity in 6% PCL and 7% PCL (Fig. 2d). These results suggested that the 6% PCL and 7% PCL had higher wall porosity, potentially promoting cell infiltration, nutrient diffusion, tissue regeneration, and remodeling. Considering the need to form a microvascular network after subsequent endothelial cell inoculation, we further analyzed that the effective porosity in the PCL-tube revealed that the 6% PCL group revealed significantly higher porosity compared to the other concentrations (Fig. 2e). These intricately linked pores enhanced substance diffusion and nutrient transport in culture, which could impact the long-term culture of engineered tissues. To validate the mechanical suitability of PCL-tubes, axial tensile tests were performed across four concentrations (ESI Fig. 1†). The Young's modulus exhibited a concentration-dependent increase with rising PCL content, progressing from 1.58 MPa at 6% PCL to 1.84 MPa at 9% PCL, indicating enhanced material rigidity at higher filler loadings. Given the mechanical properties and the effective porosity, 6% PCL was selected for subsequent experiments.

To evaluate the cellular activity of HUVECs within PCL-tubes, cells were cultured on 6% PCL-tubes and tissue culture plates (TCP) as the control. After culturing for 24 h, the Live/Dead fluorescence assay results showed that there was no significant difference in cell viability when HUVECs were cultured within 6% PCL (98.4% ± 1.3%) and the TCP group (98.4% ± 0.3%) (ESI Fig. 2†). HUVECs in PCL-tubes exhibited characteristic spreading morphology with predominant green fluorescence, demonstrating maintained viability (Fig. 2f). Confocal microscopy confirmed the formation of a continuous endothelial monolayer within PCL-tubes. These results demonstrated the non-cytotoxicity and biocompatibility of PCL-tubes.

Moreover, the phase-separated process created a porous tube wall with a high specific surface area-to-volume ratio, providing an appropriate environment for HUVEC adhesion and survival.

3.2 Biocompatibility and permeability assessment of ECs-PCL-tubes

To demonstrate the formation of stable vasculature, endothelial maturation was firstly assessed by examining the expression of key endothelial markers. We used PCL-tubes as a scaffold for large vessels and seeded HUVECs into the PCL-tubes to allow cells to self-assemble into a microvascular network over 3 days to prepare multi-scale ECs-PCL-tubes. Importantly, after 3 days of culturing, these endothelial cells maintained endothelial phenotype and remained confluent, characterized by high expression of CD31, confirming functional endothelialization (ESI Fig. 3a†). Strong VE-cadherin expression (ESI Fig. 3b†) confirmed stable intercellular junctions, critical for endothelial barrier integrity. These results established that robust junctional complexes supported endothelial monolayer integrity, essential for vascular functionality.

To evaluate the vascular barrier function, we embedded ECs-PCL-tubes within GelMA and performed permeability assays using 70 kDa FITC-dextran. The ECs-PCL-tube was created by coating PCL-tubes with confluent HUVEC layers over 3 days prior to GelMA encapsulation. For comparison, PCL-tubes without endothelial coating were similarly embedded in GelMA as controls (the PCL-tube group). Both configurations were perfused with FITC-dextran according to the experimental scheme illustrated in Fig. 3a. Following FITC-dextran loading, the fluorescent tracer fully occupied the luminal spaces. Fig. 3b shows the progressive dextran migration from the lumen to the GelMA matrix in the PCL-tube of the control group. The diffusion permeability was shown by the gray level of the fluorescence intensity at a specific position along the axis of the lumen. The gray level of the PCL-tube group distribution became broader and more dispersed over time, indicating unrestricted diffusion (Fig. 3c). In contrast, the ECs-PCL-tube maintained remarkable stability in fluorescence intensity profiles along the lumen axis. The diffusion of FITC-dextran in the PCL-tube group was significantly faster compared to the ECs-PCL-tube (Fig. 3d). The ECs-PCL-tube group exhibited negligible temporal dispersion in fluorescence distribution patterns (Fig. 3e). Quantitative analysis of FITC-dextran (70 kDa) diffusion at t = 50 min showed that the cumulative diffusion area reached 301 197 ± 18 450 px^2 in the PCL-tube group, while the ECs-PCL-tube exhibited markedly constrained tracer spread (18 536 ± 1120 px^2). Cumulative diffusion analysis revealed a 16.25-fold greater permeability in the control *versus* the ECs-PCL-tube ($p < 0.05$), demonstrating significantly restricted macromolecular permeation in the ECs-PCL-tube compared to the control group (Fig. 3f). The constrained diffusion profile demonstrated superior macromolecular retention (70 kDa) and homogeneous permeability in the ECs-PCL-tube, confirming functional endothelialization. The 70 kDa threshold was selected to align with the physiological size exclusion limit of microvascular endothelium, thereby establishing the model's capacity to replicate *in vivo* molecular sieving functionality critical for barrier integrity.[49,50] Spatiotemporal profiling revealed sustained barrier functionality in the ECs-PCL-tube, with fluorescence intensity gradients maintained from the baseline distribution patterns. In contrast, the control group exhibited progressive signal dispersion. These findings confirmed that confluent HUVECs established restrictive paracellular junctions capable of effectively limiting 70 kDa macromolecule translocation.

3.3 Cell viability in myocardial tissue constructs with ECs-PCL-tube integration

Building upon the validated barrier functionality of ECs-PCL-tubes (Fig. 3b–f), we integrated these ECs-PCL-tubes into engineered heart tissue to establish microvascular networks. Specifically, we assembled PCL-tubes and ECs-PCL-tubes with CM-loaded FG hydrogels named Tube-Gel and ECs-Tube-Gel, with the control group of CM-loaded FG hydrogels (named Gel). The FG hydrogel provided a versatile scaffold for cardiomyocytes, promoting a more ideal 3D environment for growth, nutrient transport, and cellular maturation, significantly outperforming GelMA alone.[51] Engineered myocardial tissue was three-dimensionally cultured in FG hydrogel, demonstrating spontaneous contractility and electrophysiological synchronization (ESI, Movie 1†). The modular assembly diagram of the PCL-tube and ECs-PCL-tube and the engineered myocardium is shown in Fig. 4a.

To evaluate the biocompatibility of these constructs, we cultured the constructs for 5 days to investigate cellular viability. Live/dead staining revealed predominant CM viability in FG hydrogels (Fig. 4b–g), with the majority of live cells (green) across all groups. We selected gel-embedded cells adjacent to the PCL-tube to observe CM activity and enhance visualization. Confocal overlay images showed a significant reduction in dead cells (red) in the Tube-Gel and ECs-Tube-Gel groups (Fig. 4d and f). PCL-tube positioning (dashed outlines) was verified through z-stack reconstruction. Confocal 3D view revealed that dead cells (red) in the tissue center were significantly reduced after assembling the PCL-tube and ECs-PCL-tube (Fig. 4e and g). PCL-tube integration increased CM viability from 85.1 ± 1.0% (Gel) to 97.1 ± 0.6% (Tube-Gel) ($p < 0.05$) (Fig. 4h). These results are consistent with the assembly of large vascular scaffold PCL-tube, suggesting that their structure may facilitate nutrient infiltration and enhanced cardiomyocyte activity within FG hydrogel. Furthermore, microvascular self-organization in ECs-Tube-Gel increased CM viability by 98.6% ± 0.4%, which is potentially linked to improved oxygen and nutrient transport. Tube-Gel and ECs-Tube-Gel groups exhibited 80.8% and 90.4% reductions in dead cells compared to the Gel control (Fig. 4h). These results suggested that multi-scale ECs-PCL-tubes significantly enhanced cellular activity in the engineered myocardium and prevented nutrient perfusion-induced necrosis in 3D-cultured cardiomyocytes, maintaining 98.6% cell viability during a 5 day culture period. In previous

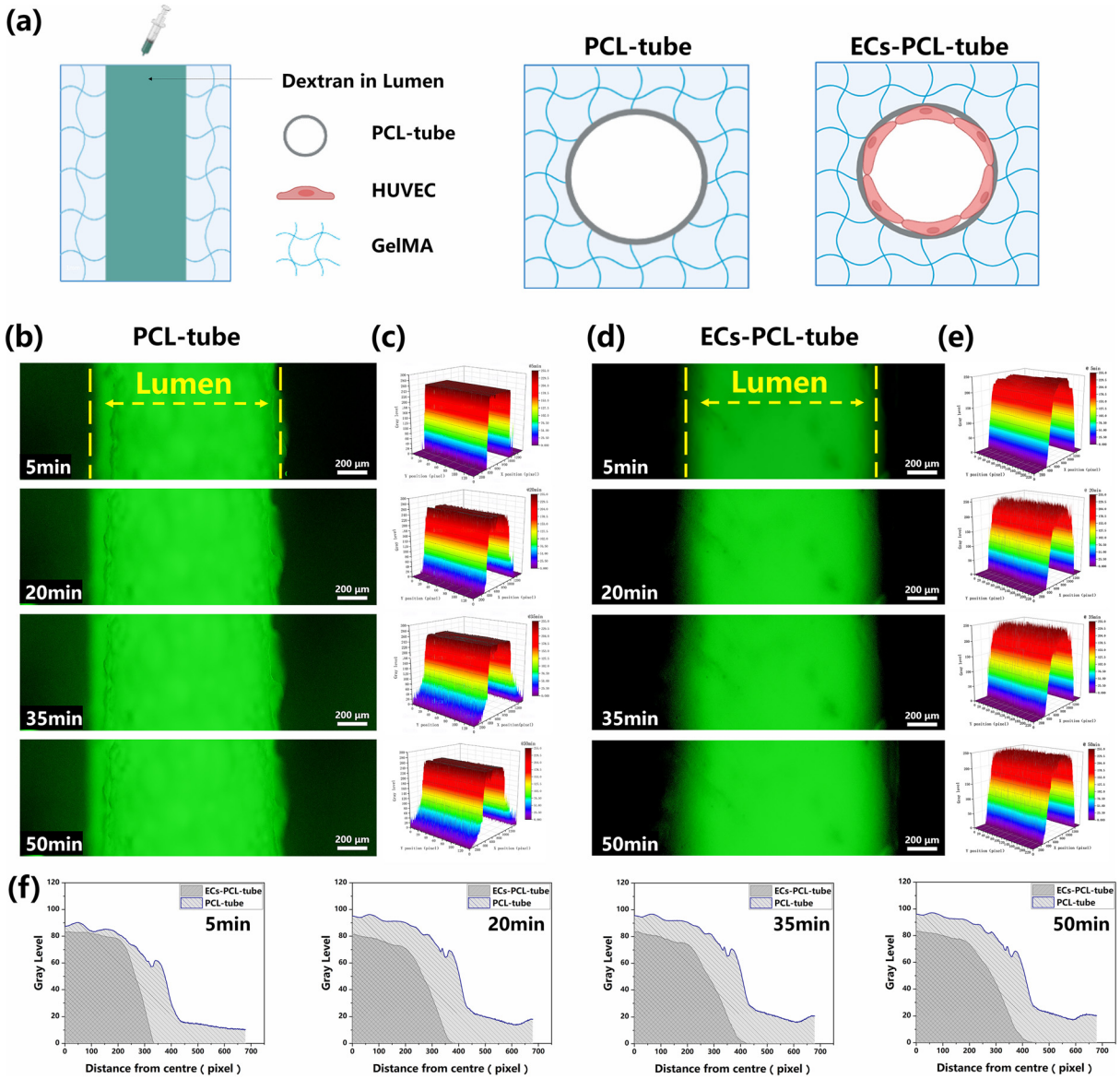

Fig. 3 Barrier function of the ECs-PCL-tubes. (a) Schematic of the diffusion permeability. The green area represents FITC-dextran in the lumen. (b) Time-lapse fluorescence images showing FITC-dextran diffusion in the PCL-tube group. The yellow dashed line represents the outer walls of the PCL-tube; time points: 5, 20, 35, and 50 min. (c) 3D grayscale heatmap of images derived from fluorescence images (PCL-tube). (d) Time-lapse fluorescence images showing FITC-dextran diffusion in the ECs-PCL-tube group. The yellow dashed line represents the outer walls of the ECs-PCL-tube. Time points: 5, 20, 35, and 50 min. (e) 3D grayscale heatmap of images derived from fluorescence images (ECs-PCL-tube). (f) Diffusion area of FITC-dextran in the PCL-tube and ECs-PCL-tube at 5, 20, 35, and 50 min time points. Scale bar: 200 μm.

studies, electrical stimulation was employed to enhance vascular network formation and maturation in the engineered myocardium.[52] However, different cell types, such as hiPSC-CMs and HUVECs, had different sensitivities to stimuli, which could lead to uneven responses. Furthermore, the long-term effects and stability of electrical stimulation still needed to be further verified. In contrast, engineered myocardial tissues developed in this study exhibited stable and functionally enhanced multiscale vascular networks *via* endothelial-mediated oxygenation and nutrient supply.

3.4 Cardiomyocyte spreading and phenotype in myocardial tissue with ECs-PCL-tubes

To evaluate the CM spreading and phenotype of these constructs, F-actin fluorescence staining and confocal imaging were performed on three groups. Following a 3-day culture period, distinct morphological differences were observed among these groups. The ECs-Tube-Gel group exhibited the most extensive cellular spreading, with the majority of CMs adopting spindle-shaped morphologies. CMs in FG hydrogels exhibited clear polarization, with actin-rich protrusions extending into the sur-

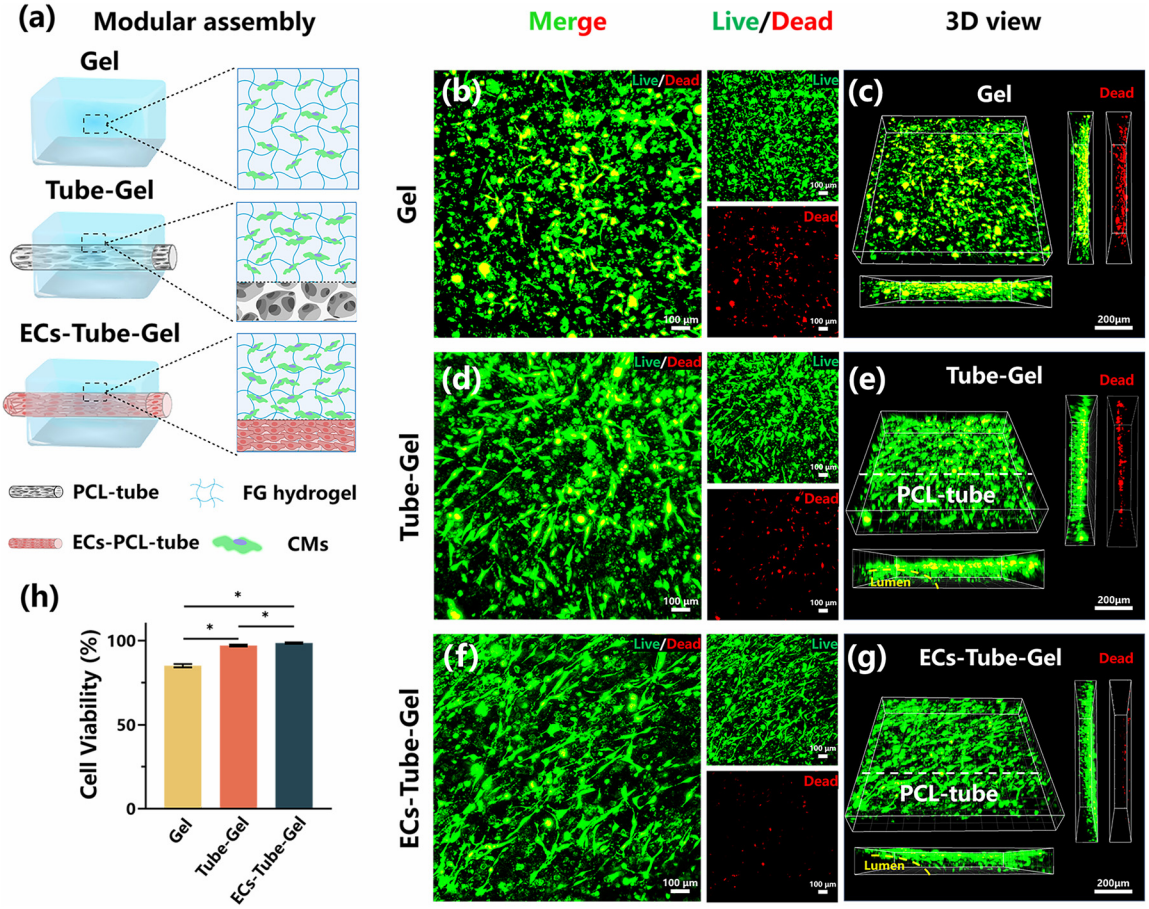

Fig. 4 Cell viability analysis of CMs encapsulated within Gel, Tube-Gel and ECs-Tube-Gel. (a) Schematic diagram of the modular assembly to construct vascularized engineered cardiac tissue. The observation site was located near the PCL-tube (below the dotted line) and within the CMs in the FG hydrogel (above the dotted line), as shown in the 3D view. (b–g) Confocal microscopy images of live/dead staining after 5-day culture, with live cells in green and dead cells in red. 3D views with multiple angles and red channel-only side views for dead cells are shown, respectively. The PCL-tube (below the dotted line) and CMs in FG hydrogels (above) in the 3D view. (h) Graph of statistical analysis of cell viability after 5 days of culture in different groups (n = 3) (*p < 0.05).

rounding hydrogel matrix. The Tube-Gel group showed partial improvement in cell spreading. In contrast, in the Gel group, CMs predominantly exhibited a rounded or slightly elliptical morphology, with F-actin fluorescence localized predominantly at the cell periphery, suggesting poor cellular spreading (Fig. 5a). Quantification of F-actin positive areas corroborated these observations. Compared to the Gel (31.6% ± 0.5%), the Tube-Gel (46% ± 1.9%) and ECs-Tube-Gel (61.1% ± 0.3%) showed distinct differences in cell spreading at 3 days, with the ECs-Tube-Gel group demonstrating enhanced CM morphology and spreading (Fig. 5b).

To further validate the role of the ECs-PCL-tube in enhancing CM spreading, we extended the culture period to 5 days. Both ECs-Tube-Gel and Tube-Gel groups exhibited significant enhancements in cytoskeletal organization. CM exhibited expanded F-actin-positive areas with elongated morphologies (Fig. 5c). The Gel group exhibited modest improvements in spreading compared to day 3, yet CMs remained predominantly rounded with poor spreading areas (Fig. 5a and c). Notably, CMs in both PCL-tube-containing groups aligned along specific axes, likely guided by the topological cues of the PCL-tube framework. This directional alignment was absent in the Gel control. We quantified F-actin positive areas and the results revealed that the Tube-Gel (53.2% ± 1.4%) and ECs-Tube-Gel (63.9% ± 1.8%) groups exhibited significantly larger spreading areas than the Gel (34.4% ± 0.9) group (Fig. 5d). The ECs-Tube-Gel group, which integrated ECs-PCL-tubes, positively impacted oxygen and nutrient transport and enhanced cell spreading within FG hydrogels. These results collectively demonstrated that the integration of the ECs-PCL-tube within FG hydrogels significantly enhanced the cell spreading within FG hydrogels, providing a promising strategy for cardiac tissue engineering applications.

3.5 Myocardial maturation in vascularized engineered cardiac tissues

To further validate our results, we examined the expression of myocardial maturation markers to evaluate the function-

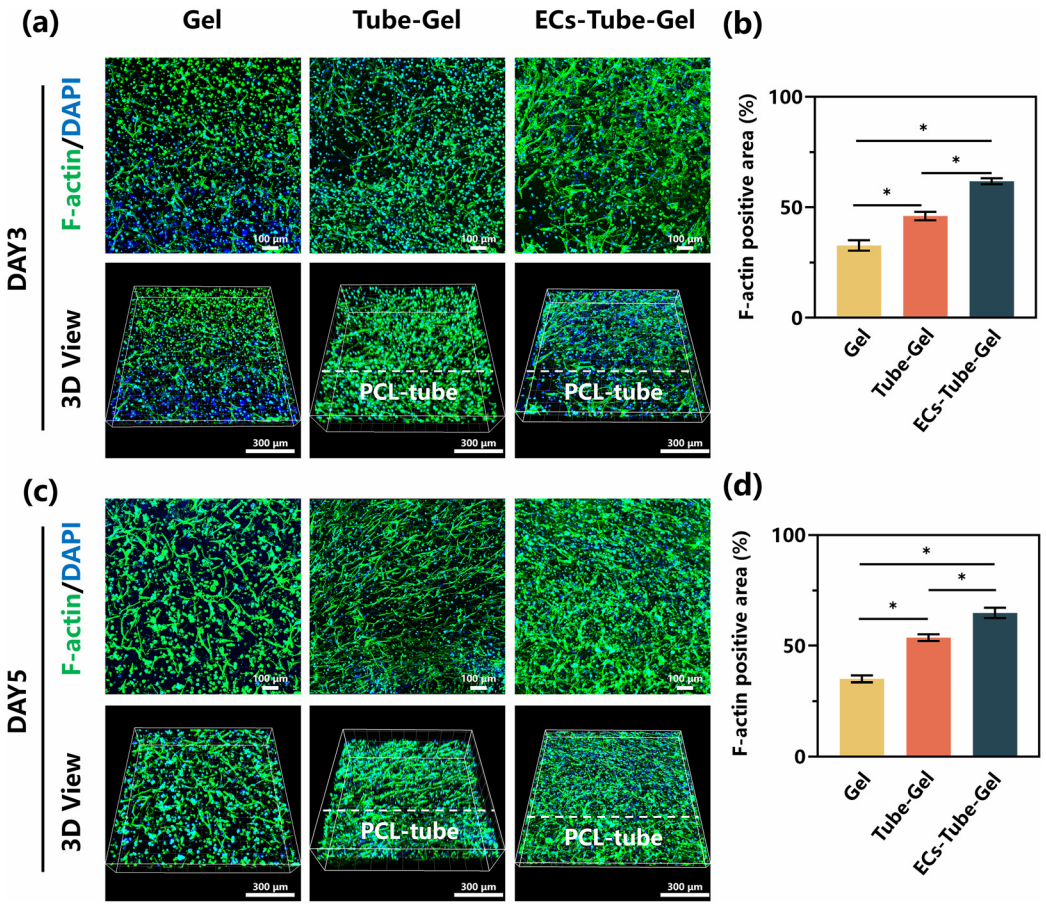

Fig. 5 Cytoskeleton morphology (F-actin, green) of CMs encapsulated within Gel, Tube-Gel and ECs-Tube-Gel. (a) Confocal images (up) and 3D views (down) of cytoskeleton staining after 3 days of culture. PCL-tube (below the dotted line) and CMs in FG hydrogels (above) in the 3D view. (b) Statistical analysis of the positive area coverage of the cytoskeleton after 3 days of culture (n = 3) (*p < 0.05). (c) Confocal images (up) and 3D views (down) of cytoskeleton staining after 5 days of culture. PCL-tube (below the dotted line) and CMs in FG hydrogels (above) in the 3D view. (d) Statistical analysis of the positive area coverage of the cytoskeleton after 5 days of culture (n = 3) (*p < 0.05).

ality of CMs within the FG hydrogels. Immunofluorescence staining for sarcomeric α-actinin, CX43, and cTnT was performed to investigate the maturation of the CMs. Confocal imaging of the Tube-Gel and ECs-Tube-Gel groups revealed that CMs within the FG hydrogels formed extensive, interconnected sarcomeric structures. In comparison with the Gel control group, well-defined Z-disc striations were clearly visible at high magnifications (Fig. 6a). The ECs-Tube-Gel form exhibited longer sarcomeres, with the formation of an interconnected α-actinin network, attributed to improved nutrient and oxygen diffusion and mechanical coupling with endothelial networks. Quantitatively, the α-actinin positive area was significantly higher in ECs-Tube-Gel (51.8 ± 1.2%) compared to Tube-Gel (42.8 ± 0.8%) and Gel (34.6 ± 1.9%) (p < 0.05, Fig. 6b). The expression of CX43, a gap junction protein crucial for electrical signaling between CMs, followed a similar trend. The CX43 expression further supported the enhanced functional integration seen in the ECs-Tube-Gel group, with ECs-Tube-Gel tissues showing dense, punctate CX43 plaques at cell–cell junctions (Fig. 6a). The Tube-Gel group exhibited an intermediate level of the CX43 positive area in ECs-Tube-Gel (20.5 ± 2.2%), which was 1.22-fold and 1.75-fold higher than Tube-Gel (16.8 ± 0.8%) and Gel (11.7 ± 0.9%) (p < 0.05) (Fig. 6c), further confirming the role of vascularized scaffolds in enhancing cardiomyocyte maturation. This higher CX43 expression indicated improved electrical coupling between adjacent CMs, which was vital for synchronous beating and functional coordination. These results aligned with the above results that ECs-Tube-Gel promoted CM spreading within the FG hydrogels, as evidenced by enhanced cell spreading (F-actin). The beating behavior of vascularized cardiac tissue was further investigated using microscopy (ESI, Movies 1–3†). In the ECs-Tube-Gel group, coordinated contractions with high synchronicity were observed across the cardiomyocyte network, consistent with the enhanced CX43 gap junction density and α-actinin expression. In contrast, the Gel group appeared sporadic with minimal intercellular coordination.

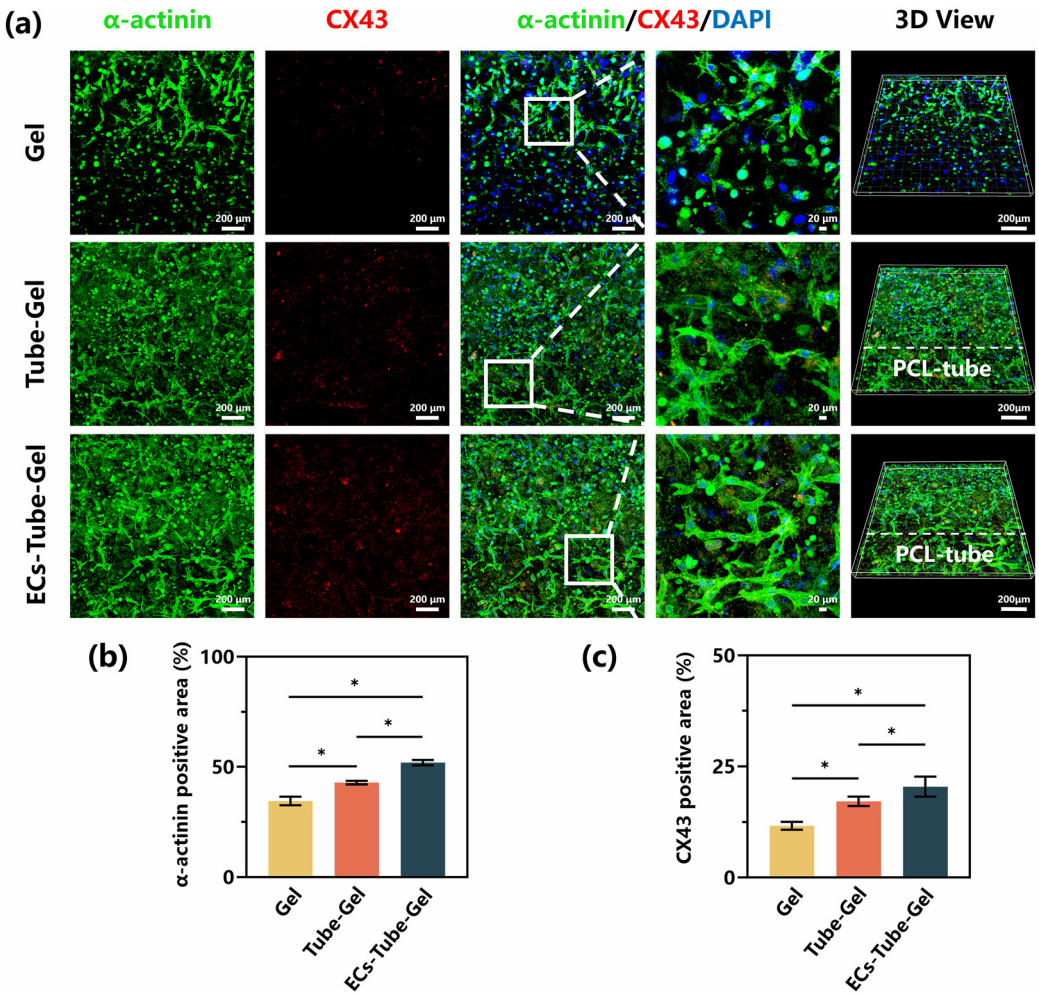

Fig. 6 Phenotype of CMs encapsulated within Gel, Tube-Gel and ECs-Tube-Gel after 5 days of culture. (a) Immunofluorescence staining of α-actinin (green), CX43 (red), and nuclei (blue) revealed that cardiac tissues in FG hydrogels and the different groups exhibited phenotypic differences. 3D views of the CMs in different scaffolds show varying amounts of ordered sarcomere structures. In the 3D view, the PCL-tube was positioned below the dotted line, while the CMs in the FG hydrogels were positioned above it. (b) Quantified analysis of the relative percentage of area coverage by α-actinin in FG hydrogels (n = 3). (c) Quantified analysis of the relative percentage of area coverage by CX43 in FG hydrogels (n = 3) (*p < 0.05).

These movies further demonstrated that electrical signals were transmitted rapidly between the mature, tightly connected CMs.

CTnT was used to evaluate the functional maturity of the CMs (Fig. 7a–c). A co-staining of cTnT and CD31 was performed to assess the integration of vascular structures within the engineered heart tissues. The cTnT staining clearly demonstrated that CMs in the ECs-Tube-Gel group had a larger and more expression compared to the other groups, suggesting enhanced contractile protein expression and functional maturation (Fig. 7c). Contrastingly, the Gel exhibited weak cTnT expression with a poorly developed cTnT positive area (Fig. 7a). The 3D view of the cTnT staining further supported these observations and further demonstrated that the PCL-tube was located below the dotted line. After culturing for 5 days, the cTnT fluorescence staining results showed that the ECs-Tube-Gel group exhibited the highest percentage of the cTnT-positive area (70.6% ± 4.9%), significantly higher than both the Tube-Gel (50.8% ± 5.6%) and Gel (31.8% ± 5.1%) (Fig. 7b; ESI Fig. 4†). This increased cTnT expression aligned with the improved contractility and maturation observed in the ECs-Tube-Gel group. The fluorescence staining experiments provided valuable insights into the maturation and functional characteristics of CMs within different groups. The ECs-Tube-Gel group exhibited superior CM sarcomere formation, gap junction expression, and contractility, as evidenced by both fluorescence microscopy and quantitative analysis. These results suggested that the presence of a vascularized PCL-tube within the hydrogel scaffold significantly enhanced the maturation of CMs, facilitating better cell–cell communication. The findings underscored the importance of ECs-PCL-tubes in engineered cardiac tissues, supporting their potential application in regenerative medicine.

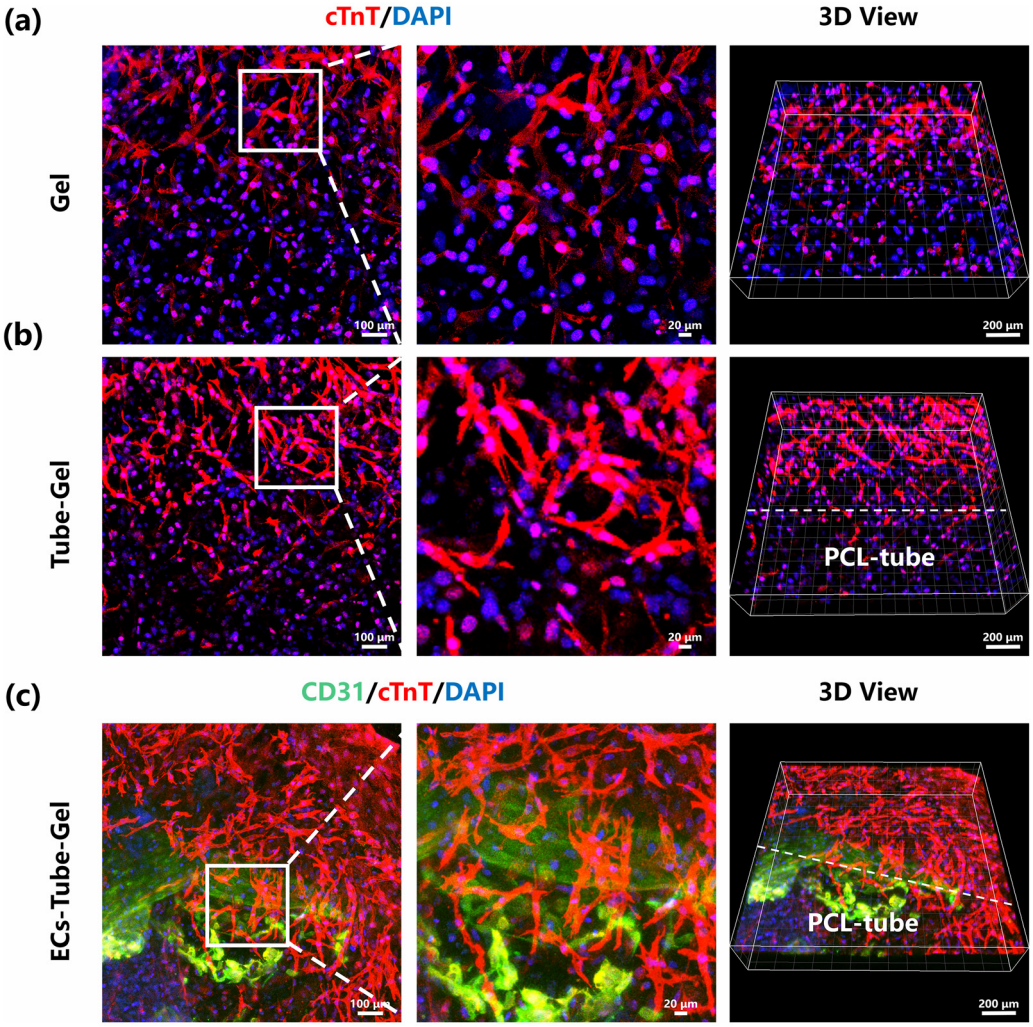

Fig. 7 Assessment of cTnT of CMs encapsulated within Gel, Tube-Gel and ECs-Tube-Gel after 5 days of culture. (a) Gel (the control group) immunofluorescence staining of cTnT (red) and the nucleus (blue) confocal images and 3D view. (b) Tube-Gel immunofluorescence staining of cTnT (red) and the nucleus (blue) confocal images and 3D view. (c) ECs-Tube-Gel immunofluorescence staining of CD31 (green), cTnT (red) and the nucleus (blue) confocal images and 3D view.

4 Conclusions

In summary, we developed a PCL-tube using a combined 3D printing and phase separation strategy. Unlike conventional single-process methods, our approach uniquely combined the structural precision of 3D printing with the biomimetic porosity of phase separation. This strategy provided a scalable platform that simultaneously addressed structural hierarchy and vascular integration. We further combined it with HUVECs to construct a multi-scale ECs-PCL-tube to address critical limitations in nutrient perfusion for the engineered myocardium. The PCL-tube demonstrated stable mechanical properties, biocompatibility, and a porous architecture that promoted endothelial cell adhesion and microvascular self-assembly. The integration of an ECs-PCL-tube with CM-loaded FG hydrogel *via* modular assembly significantly improved cell viability, maturation, and functional synchronization. Notably, the ECs-PCL-tube established a functional barrier that mimics physiological vascular permeability, while its hierarchical porosity facilitated efficient nutrient diffusion. Modular assembly of ECs-PCL-tubes with the engineered myocardium reduced central necrosis in 3D cultures and achieved over 98% cardiomyocyte viability after 5 days. Furthermore, the increased expression of cardiac maturation markers including α-actinin, CX43, and cTnT was observed. Synchronized beating behavior highlighted the ability of ECs-PCL-tubes to promote intercellular communication and electromechanical coupling. The scalable and cost-effective modular assembly strategy offered a promising platform for constructing vascular cardiac tissues *in vitro*. Our work advanced vascularized cardiac tissue engineering and demonstrated significant potential for regenerative medicine and drug screening. Future studies will aim to optimize vascular network integration across multiple scales and validate long-term functionality in dynamic culture systems.

Ethical statement

All animal procedures were performed in accordance with the Guidelines for Care and Use of Laboratory Animals of Southern Medical University and approved by the Animal Ethics Committee of Southern Medical University.

Conflicts of interest

The authors declare that they have no known competing financial interests or personal relationships that could have appeared to influence the work reported in this paper.

Data availability

All data generated or analysed during this study are included in this published article and its ESI.†

Acknowledgements

This work was financially supported by the National Key Research and Development Program of China (grant no. 2022YFB4600600).

References

1 A. F. Jebran, T. Seidler, M. Tiburcy, M. Daskalaki, I. Kutschka, B. Fujita, S. Ensminger, F. Bremmer, A. Moussavi, H. Yang, X. Qin, S. Mißbach, C. Drummer, H. Baraki, S. Boretius, C. Hasenauer, T. Nette, J. Kowallick, C. O. Ritter, J. Lotz, M. Didié, M. Mietsch, T. Meyer, G. Kensah, D. Krüger, M. S. Sakib, L. Kaurani, A. Fischer, R. Dressel, I. Rodriguez-Polo, M. Stauske, S. Diecke, K. Maetz-Rensing, E. Gruber-Dujardin, M. Bleyer, B. Petersen, C. Roos, L. Zhang, L. Walter, S. Kaulfuß, G. Yigit, B. Wollnik, E. Levent, B. Roshani, C. Stahl-Henning, P. Ströbel, T. Legler, J. Riggert, K. Hellenkamp, J. U. Voigt, G. Hasenfuß, R. Hinkel, J. C. Wu, R. Behr and W. H. Zimmermann, *Nature*, 2025, **639**, 503–511.

2 S. Cho, D. E. Discher, K. W. Leong, G. Vunjak-Novakovic and J. C. Wu, *Nat. Methods*, 2022, **19**, 1064–1071.

3 J. Zhang, J. Li, X. Qu, Y. Liu, L. Sun, A. Harada, Y. Hua, N. Sougawa, A. Tabata, L. Liu and S. Miyagawa, *Bioact. Mater.*, 2024, **37**, 533–548.

4 M. Hashemi, F. B. Finklea, H. Hammons, Y. Tian, N. Young, E. Kim, C. Halloin, W. Triebert, R. Zweigerdt, A. K. Mitra and E. A. Lipke, *Bioact. Mater.*, 2025, **43**, 423–440.

5 P. Chen, W. Zhang, X. Fan, X. Shi, Y. Jiang, L. Yan, H. Li, C. Wang, L. Han, X. Lu and C. Ou, *Nano Today*, 2024, **55**, 102157.

6 D. G. Hwang, H. Choi, U. Yong, D. Kim, W. Kang, S. M. Park and J. Jang, *Adv. Mater.*, 2024, **36**, e2400364.

7 H. Li, I. Shadrin, A. Helfer, K. Heman, L. Rao, C. Curtis, G. M. Palmer and N. Bursac, *Acta Biomater.*, 2024, DOI: **10.1016/j.actbio.2024.11.014**.

8 X. Jia, W. Liu, Y. Ai, S. Cheung, W. Hu, Y. Wang, X. Shi, J. Zhou, Z. Zhang and Q. Liang, *Adv. Mater.*, 2024, **36**, 2404071.

9 Z. Wang, S. M. Mithieux and A. S. Weiss, *Adv. Healthc. Mater.*, 2019, **8**, e1900742.

10 S. Grebenyuk, A. Rahman Abdel Fattah, M. Kumar, B. Toprakhisar, G. Rustandi, A. Vananroye, I. Salmon, C. Verfaillie, M. Grillo and A. Ranga, *Nat. Commun.*, 2023, **14**, 193.

11 W. Song, A. Chiu, L.-H. Wang, R. E. Schwartz, B. Li, N. Bouklas, D. T. Bowers, D. An, S. H. Cheong, J. A. Flanders, Y. Pardo, Q. Liu, X. Wang, V. K. Lee, G. Dai and M. Ma, *Nat. Commun.*, 2019, **10**, 4602.

12 N. Noor, A. Shapira, R. Edri, I. Gal, L. Wertheim and T. Dvir, *Adv. Sci.*, 2019, **6**, 1900344.

13 M. A. Redd, N. Zeinstra, W. Qin, W. Wei, A. Martinson, Y. Wang, R. K. Wang, C. E. Murry and Y. Zheng, *Nat. Commun.*, 2019, **10**, 584.

14 D. Wang, S. Maharjan, X. Kuang, Z. Wang, L. S. Mille, M. Tao, P. Yu, X. Cao, L. Lian, L. Lv, J. J. He, G. Tang, H. Yuk, C. K. Ozaki, X. Zhao and Y. S. Zhang, *Sci. Adv.*, 2022, **8**, eabq6900.

15 C. Quintard, E. Tubbs, G. Jonsson, J. Jiao, J. Wang, N. Werschler, C. Laporte, A. Pitaval, T.-S. Bah, G. Pomeranz, C. Bissardon, J. Kaal, A. Leopoldi, D. A. Long, P. Blandin, J.-L. Achard, C. Battail, A. Hagelkruys, F. Navarro, Y. Fouillet, J. M. Penninger and X. Gidrol, *Nat. Commun.*, 2024, **15**, 1452.

16 C. D. Roche, P. Sharma, A. W. Ashton, C. Jackson, M. Xue and C. Gentile, *Front. Bioeng. Biotechnol.*, 2021, **9**, 636257.

17 O. King, D. Cruz-Moreira, A. Sayed, F. Kermani, W. Kit-Anan, I. Sunyovszki, B. X. Wang, B. Downing, J. Fourre, D. Hachim, A. M. Randi, M. M. Stevens, M. Rasponi and C. M. Terracciano, *Cells Rep. Methods*, 2022, **2**, 100280.

18 L. Xu, M. Varkey, A. Jorgensen, J. Ju, Q. Jin, J. H. Park, Y. Fu, G. Zhang, D. Ke, W. Zhao, R. Hou and A. Atala, *Biofabrication*, 2020, **12**, 045012.

19 P. Wang, Y. Sun, X. Shi, H. Shen, H. Ning and H. Liu, *Bio-Des. Manuf.*, 2021, **4**, 344–378.

20 X. Cao, R. Ashfaq, F. Cheng, S. Maharjan, J. Li, G. Ying, S. Hassan, H. Xiao, K. Yue and Y. S. Zhang, *Adv. Funct. Mater.*, 2019, **29**, 1807173.

21 I. Goldfracht, M. Machour, I. Michael, M. Bulatova, J. Zavin and S. Levenberg, *Adv. Funct. Mater.*, 2025, **35**, 2410311.

22 S. C. Neves, A. Sousa, D. S. Nascimento, I. D. Orge, S. A. Ferreira, C. Mota, L. Moroni, C. C. Barrias and P. L. Granja, *Mater. Today Bio*, 2024, **29**, 101291.

23 Q. Ge, Z. Chen, J. Cheng, B. Zhang, Y. F. Zhang, H. Li, X. He, C. Yuan, J. Liu, S. Magdassi and S. Qu, *Sci. Adv.*, 2021, **7**, eaba4261.

24 P. P. Stankey, K. T. Kroll, A. J. Ainscough, D. S. Reynolds, A. Elamine, B. T. Fichtenkort, S. G. M. Uzel and J. A. Lewis, *Adv. Mater.*, 2024, **36**, e2401528.

25 M. Mao, K. Han, J. Gao, Z. Ren, Y. Zhang, J. He and D. Li, *Adv. Mater.*, 2025, **37**, 2419380.
26 J. Nie, Q. Gao, C. Xie, S. Lv, J. Qiu, Y. Liu, M. Guo, R. Guo, J. Fu and Y. He, *Mater. Horiz.*, 2020, **7**, 82–92.
27 Z. Wang, L. Wang, T. Li, S. Liu, B. Guo, W. Huang and Y. Wu, *Theranostics*, 2021, **11**, 7948–7969.
28 F. Maiullari, M. Costantini, M. Milan, V. Pace, M. Chirivì, S. Maiullari, A. Rainer, D. Baci, H. E. Marei, D. Seliktar, C. Gargioli, C. Bearzi and R. Rizzi, *Sci. Rep.*, 2018, **8**, 13532.
29 Z. Gu, M. Xie, S. Lv, N. Liu, J. He, Y. Li, Y. Zhu, J. Fu, H. Lin, C. Xie and Y. He, *Int. J. Bioprint.*, 2022, **8**, 619.
30 D. Xue, Y. Wang, J. Zhang, D. Mei, Y. Wang and S. Chen, *ACS Appl. Mater. Interfaces*, 2018, **10**, 19428–19435.
31 Q. Gao, Z. Liu, Z. Lin, J. Qiu, Y. Liu, A. Liu, Y. Wang, M. Xiang, B. Chen, J. Fu and Y. He, *ACS Biomater. Sci. Eng.*, 2017, **3**, 399–408.
32 A. A. Szklanny, M. Machour, I. Redenski, V. Chochola, I. Goldfracht, B. Kaplan, M. Epshtein, H. Simaan Yameen, U. Merdler, A. Feinberg, D. Seliktar, N. Korin, J. Jaroš and S. Levenberg, *Adv. Mater.*, 2021, **33**, e2102661.
33 J. Fang, H. Liu, W. Qiao, T. Xu, Y. Yang, H. Xie, C. H. Lam, K. W. K. Yeung and X. Zhao, *Adv. Healthc. Mater.*, 2023, **12**, e2201220.
34 X. Yang, S. Li, X. Sun, Y. Ren, L. Qiang, Y. Liu, J. Wang and K. Dai, *Int. J. Bioprint.*, 2023, **9**, 749.
35 J. Son, S. J. Hong, J. W. Lim, W. Jeong, J. H. Jeong and H. W. Kang, *Small Methods*, 2021, **5**, e2100632.
36 Z. Dong, H. Cui, H. Zhang, F. Wang, X. Zhan, F. Mayer, B. Nestler, M. Wegener and P. A. Levkin, *Nat. Commun.*, 2021, **12**, 247.
37 B. Stolz, M. Mader, L. Volk, T. Steinberg and R. Mülhaupt, *Macromol. Mater. Eng.*, 2021, **306**, 2000541.
38 P. X. Ma and R. Zhang, *J. Biomed. Mater. Res.*, 1999, **46**, 60–72.
39 V. van Duinen, A. van den Heuvel, S. J. Trietsch, H. L. Lanz, J. M. van Gils, A. J. van Zonneveld, P. Vulto and T. Hankemeier, *Sci. Rep.*, 2017, **7**, 18071.
40 J. Chen, D. Huang, L. Wang, J. Hou, H. Zhang, Y. Li, S. Zhong, Y. Wang, Y. Wu and W. Huang, *J. Colloid Interface Sci.*, 2020, **574**, 162–173.
41 L. Wang, T. Li, Z. Wang, J. Hou, S. Liu, Q. Yang, L. Yu, W. Guo, Y. Wang, B. Guo, W. Huang and Y. Wu, *Biomaterials*, 2022, **285**, 121537.
42 N. Kong, H. Yang, R. Tian, G. Liu, Y. Li, H. Guan, Q. Wei, X. Du, Y. Lei, Z. Li, R. Cao, Y. Zhao, X. Wang, K. Wang and P. Yang, *Bone Res.*, 2022, **10**, 28.
43 D. Zhi, Q. Cheng, A. C. Midgley, Q. Zhang, T. Wei, Y. Li, T. Wang, T. Ma, M. Rafique, S. Xia, Y. Cao, Y. Li, J. Li, Y. Che, M. Zhu, K. Wang and D. Kong, *Sci. Adv.*, 2022, **8**, eabl3888.
44 H. Bao, Y. Zhang, H. Xin, Y. Gao, Y. Hou, G. Yue, N. Wang, Y. Wang, C. Li, F. Liu, Y. Zhao and L. Kong, *ACS Omega*, 2024, **9**, 7609–7620.
45 J. Hou, J. Jiang, H. Guo, X. Guo, X. Wang, Y. Shen and Q. Li, *RSC Adv.*, 2020, **10**, 10055–10066.
46 P. Lemieux, S. V. Vinogradov, C. L. Gebhart, N. Guérin, G. Paradis, H. K. Nguyen, B. Ochietti, Y. G. Suzdaltseva, E. V. Bartakova, T. K. Bronich, Y. St-Pierre, V. Y. Alakhov and A. V. Kabanov, *J. Drug Targeting*, 2000, **8**, 91–105.
47 A. Afshar, H. Majd, A. Harker and M. Edirisinghe, *J. Drug Delivery Sci. Technol.*, 2024, **95**, 105582.
48 C. O'Connor, E. Brady, Y. Zheng, E. Moore and K. R. Stevens, *Nat. Rev. Mater.*, 2022, **7**, 702–716.
49 J. Nie, Q. Gao, Y. Wang, J. Zeng, H. Zhao, Y. Sun, J. Shen, H. Ramezani, Z. Fu, Z. Liu, M. Xiang, J. Fu, P. Zhao, W. Chen and Y. He, *Small*, 2018, **14**, e1802368.
50 W. Yuan, Y. Lv, M. Zeng and B. M. Fu, *Microvasc. Res.*, 2009, **77**, 166–173.
51 E. S. Lisboa, C. Serafim, W. Santana, V. L. S. dos Santos, R. L. C. de Albuquerque-Junior, M. V. Chaud, J. C. Cardoso, S. Jain, P. Severino and E. B. Souto, *J. Controlled Release*, 2024, **365**, 617–639.
52 B. Lu, M. Ye, J. Xia, Z. Zhang, Z. Xiong and T. Zhang, *Adv. Healthcare Mater.*, 2023, **12**, e2300607.